



Searching for low thermal conductivity materials for thermal barrier coatings: A theoretical approach

Majid Zeraati ,* Artem R. Oganov ,† and Tao Fan 

Skolkovo Institute of Science and Technology, Bolshoy Boulevard 30, Bld. 1, 121205 Moscow, Russia

Sergey F. Solodovnikov 

*Nikolaev Institute of Inorganic Chemistry, Siberian Branch,
Russian Academy of Sciences, Akademika Lavrentyeva Ave. 3, 630090 Novosibirsk, Russia*

 (Received 7 July 2023; revised 6 November 2023; accepted 5 February 2024; published 6 March 2024)

Low thermal conductivity is important for thermal barrier coatings, thermoelectrics, and other applications in industry and materials science. Accurate calculation of their thermal conductivity κ at high temperatures remains challenging: methods such as the Boltzmann transport equation (BTE) usually underestimate the actual value. Here we used the effective harmonic method and homogeneous nonequilibrium molecular dynamics simulations with machine-learning potentials to calculate the thermal conductivity of candidate materials at temperatures up to 1500 K. The results obtained for $\text{La}_2\text{Zr}_2\text{O}_7$, ZrSiO_4 , and BaZrO_3 are in perfect agreement with the experiment at all temperatures. We used renormalized second- and third-order interatomic force constants and phonons at high temperatures to calculate the thermal conductivity using the BTE and confirmed these results with molecular dynamics simulations. Investigating the relationship of thermal conductivity with the elastic properties, Debye temperature, and the speed of sound, we proposed threshold values for future high-throughput screening for low- κ materials. Using the molecular dynamics method at high temperatures, we calculated the volumetric thermal expansion coefficient and selected ten candidate materials for thermal barrier coatings at high temperatures. Besides thermal barrier coating materials, this approach can be applied to multiple classes of materials where thermal conductivity is important.

DOI: [10.1103/PhysRevMaterials.8.033601](https://doi.org/10.1103/PhysRevMaterials.8.033601)

I. INTRODUCTION

With the development of technology and science, gas turbines became extensively used in industry and transport. The working temperatures of stationary and aviation gas turbines are usually very high (up to 1500 K and higher), necessitating the use of thermal barrier coating (TBC) ceramics to protect turbine blades/vanes from hot gases and an oxidative atmosphere. TBCs must have high melting points, low thermal conductivity, a relatively high thermal expansion coefficient (TEC), thermal shock resistance during thermal cycling, high phase, thermal and chemical stability under oxidizing conditions, and strong adhesion to the substrate [1–3]. Currently, the most widely used materials for TBCs are yttria-stabilized zirconia (YSZ) and rare earth-doped ceria (RE-doped ceria). YSZ is a ceramic material composed of zirconia (ZrO_2) with 6–8 wt.% yttria (Y_2O_3). Its low thermal conductivity (~ 2 W/(m.K) at 1273 K), a high linear TEC ($11 \times 10^{-6} \text{ K}^{-1}$ at 293–1273 K), good thermal shock resistance, and excellent chemical stability could make it an ideal choice for TBCs [1]. However, phase transition at 1150°C–1200°C and high oxygen diffusion limit the number of thermal cycles and operating temperature

at 1200°C for YSZ. Thus increasing the working gas temperature to 1300°C and higher for the next generation of gas turbines requires the development of new materials for TBCs. Many candidates have been investigated and tested, mainly among refractory oxides based on Al_2O_3 , TiO_2 , ZrO_2 , HfO_2 , Ta_2O_5 , rare earth, and alkali earth oxides, such as fluorites ($\text{Ce}, \text{Ln})\text{O}_{2-x}$, pyrochlores $\text{A}_2^{3+}\text{B}_2^{4+}\text{O}_7$, garnets $\text{Ln}_3\text{Al}_5\text{O}_{12}$, perovskites $\text{A}^{2+}\text{B}^{4+}\text{O}_3$ and LnAlO_3 , magnetoplumbites ($\text{CaAl}_{12}\text{O}_{19}$, $\text{LaMgAl}_{11}\text{O}_{19}$), monazites LnPO_4 etc [1–5]. Pyrochlores $\text{Ln}_2\text{Zr}_2\text{O}_7$ and $(\text{Ln}, \text{Ln}')_2\text{Zr}_2\text{O}_7$ ($\text{Ln}, \text{Ln}' = \text{La}, \text{Nd}, \text{Sm}, \text{Gd}, \text{Yb}$) with relatively low oxygen diffusion, thermal conductivity of 1.1–1.7 W/(m K) and higher thermal stability than YSZ are considered to be among the most promising. Magnetoplumbites and perovskites also have a wider operating temperature range and lower thermal conductivity compared to YSZ. Nevertheless, materials that would surpass YSZ in all respects have not yet been found.

Thermal conductivity, a key property of TBC materials, is highly dependent on temperature, the size of the system, its impurities, and dislocations. However, it can be challenging to measure thermal conductivity for numerous materials. Therefore effective screening strategies are needed for choosing new stable materials with low thermal conductivity at high temperatures. Recently, considerable efforts have been made to predict such materials [2,6,7].

Machine learning (ML) and artificial intelligence (AI) can be used for high-throughput screening to select suitable

*Majid.Zeraati@skoltech.ru

†A.Oganov@skoltech.ru

candidates among the materials for thermal applications. For example, Seko *et al.* showed that by using selected features that have the highest correlation with the thermal conductivity, including atomic number, atomic mass, atomic radius, ionization energy, unit cell volume, atomic density, and vibrational density of state (DOS), the thermal conductivity of materials can be predicted with high accuracy [8]. In a high-throughput screening study, Chi *et al.* investigated 63 properties and selected 29 of them that have the greatest effect on the prediction of the thermal conductivity of inorganic materials [9]. Babaei *et al.* developed a machine learning potential (MLP) for silicon with vacancies to predict its thermal conductivity [10]. However, due to the lack of experimental data for thermal conductivity of materials in wide temperature ranges, it is difficult to train and evaluate directly machine learning models for screening thermal conductivity of materials. So, in this paper, we decided to utilize MLPs to accelerate calculation of the thermal conductivity of materials.

In this paper, we used MLPs to calculate the thermal conductivity, thermal expansion, and elastic constants of refractory oxides with fairly symmetric and complex structures, some of which are already used as TBC materials, whereas others may be considered as possible candidates for TBC applications.

The initial criteria for selecting promising phases were crystal chemical considerations that directly follow from the main requirements for materials for TBCs: high thermal stability, TEC, mechanical strength, and low thermal conductivity, which significantly limit the possible composition and structure of such a material. In terms of chemical bonding, high temperature stability and strength are associated with strong (covalent) bonds, while the other two properties are determined by weaker ionic bonds. These contradictory requirements can be satisfied by choosing complex oxides with alternating strong and weak chemical bonds (or hard and soft structural units) [3]. This means a combination in the structure of fairly small and valence-stable highly charged *B* cations (Al^{3+} , Zr^{4+} , Nb^{5+} , etc.), usually octahedrally coordinated, with large *A* cations (alkaline earth or rare earth ions) with higher coordination. It is desirable to bind the polyhedra of small cations into an extended spatial construction, which ensures the strength and thermal stability of the structure. Therefore, from the point of view of increasing the strength of the structure and isotropy of the TEC, preventing cracks in TBCs, flexible highly symmetrical framework structures with minimal cleavage and evenly distributed strong bonds are preferable, such as cubic structures of perovskite ABO_3 , pyrochlore $\text{A}_2\text{B}_2\text{O}_7$, garnet $\text{A}_3\text{B}_2\text{C}_3\text{O}_{12}$, as well as some hexagonal, tetragonal and other phases, some of which we are considered in this paper.

II. METHODS

In recent decades, several computational methods have developed for calculating thermal conductivity of crystal and amorphous materials. For example, there are several methods based on molecular dynamics (MD) simulations, including nonequilibrium molecular dynamics (NEMD) [11–13], the

Green-Kubo method [14,15], homogeneous nonequilibrium molecular dynamics (HNEMD) method [16,17]. For crystalline materials, the Boltzmann transport equation (BTE) [18–20], and for mesoscale structures and interfaces between systems the nonequilibrium Green's function (NEGF) method [21] is utilized.

Normally, the methods used for solving the Boltzmann transport equation and calculating the thermal conductivity in TBC materials are based on simplified approaches, such as the Clark model [22], Callaway model [23,24], or Slack model [25]. Most of these methods find thermal conductivity $\kappa \propto T^{-1}$, while experiments on many TBC materials have shown that at high temperatures, their thermal conductivity is weakly dependent on temperature [26–28], which is expected more of amorphous materials than crystals. Several new theoretical studies have been conducted to unify the propagative and diffusive mechanisms of thermal conductivity in amorphous and crystalline materials to explain this behavior [29–32].

In this study, we applied two approaches to calculate thermal conductivity of materials: solving the BTE using the temperature-dependent interatomic force constants (TDIFCs) in the effective harmonic model (EHM) [33,34], and homogeneous nonequilibrium molecular dynamics simulations [16,17]. The best approach to achieve high accuracy in MD simulation or calculating the second- and third-order interatomic force constants (IFCs) [35,36] which are required in BTE, is using density functional theory (DFT). This approach has high accuracy but is computationally expensive. An ideal strategy is to use MLPs in molecular dynamics simulations and calculation of the IFCs [37–41]. The accuracy is comparable to DFT, whereas the computational cost is much lower. To calculate the IFCs, thermal expansion (using MD simulations), and elastic constants, we used the moment tensor potential (MTP) [42–45] as implemented in MLIP package [46]. In the HNEMD method, we used a new neuroevolution potential (NEP) [47–49], which is implemented in the GPUMP package [50].

A. Machine learning potentials

We need ML potentials that would enable us to reliably perform simulations at temperatures between 100 and approximately 2000 K. To achieve this, first, we used the D-optimality-based active learning method [43,44] to train the moment tensor potentials.

At the first step of active learning, we generated initial training sets by selecting 100 trajectories from short AIMD calculations at room temperature. We used AIMD as implemented in the VASP code [51] with projector-augmented wave (PAW) potentials [52] and the Perdew–Burke–Ernzerhof (PBE) generalized gradient approximation exchange–correlation functional [53]. All AIMD calculations were performed on different supercells and *k*-point grids [54] using the *NPT* ensemble [55,56]. The corresponding values for each material are provided in Ref. [57] (see Table SI). Plane waves up to an energy cutoff of 600 eV were used as a basis set to represent the Kohn–Sham wave functions. The time step was 2 fs, and the total simulation time for AIMD was 6 ps.

After preparing the initial training set, we proceeded to the initial training of the moment tensor potential with a cutoff radius of 6 Å. Using the obtained initial potential, we performed classical molecular dynamics simulations with the *NPT* ensemble gradually from zero to 2000 K for 10 ps and then a simulation at fixed $T = 2000$ K for 5 ps. During this simulation, we selected new configurations using the active learning method and added them to the training set after running them with DFT and retraining the potential. We continued these steps until no new configurations were selected. To perform classical molecular dynamics calculations, we used the large-scale atomic/molecular massively parallel simulator (LAMMPS) package [58] with the MLIP code.

The same training sets were employed to train the neuroevolution potentials. For some materials having high symmetry and stability at higher temperatures, NEP2-type potentials with a cutoff radius of 6 Å were used [48], whereas other materials were simulated using NEP3-type potentials with a cutoff radius of 8 Å [49]. One of the reasons for using the NEPs in calculating the thermal conductivity through molecular dynamics simulations was the much higher computational speed of these potentials compared to the MTP. NEPs enable us to perform simulations at large system sizes (about 30 000 atoms in the simulation box) and very long simulation times (about 3 ns), which are required to reach a converged value of thermal conductivity using MD.

The validation of the trained machine learning potentials was performed using 100 randomly selected configurations that were generated during molecular dynamics simulations (not included in the training sets). The average errors in the energies, forces, and stresses, and the number of configurations in the active training set for each potential are provided in Ref. [57] (Table SI).

To validate the MLIPs capabilities in computing lattice dynamics of materials, we relaxed the unit cells using the BFGS optimization method and the moment tensor potentials, and then calculated the phonon dispersion curves using PHONOPY package [59] interfaced with MLIP code. Tests for four materials show that the phonon dispersion curves calculated using DFT are accurately reproduced using the MTPs (Fig. 1).

B. Thermal conductivity

Calculating thermal conductivity of TBC materials poses a significant challenge. TBC materials are insulators and their thermal conductivity is predominantly due to phonons (lattice thermal conductivity). In this study, we first calculate lattice thermal conductivity using the phonon gas model by solving the BTE [18,20], and then investigate the limitations of this approach and ways to overcome them for complex anharmonic materials at high temperatures.

We used an iterative self-consistent algorithm [20] as implemented in the SHENGBTE package [36] for solving the BTE. In the calculations, we considered third-order interatomic force constants up to the fourth nearest neighbor in a supercell [35]. The size of supercells for each structure is presented in Ref. [57] Table SII.

As a second approach, we used specialized thermostats in the homogeneous nonequilibrium molecular dynamics approach [16,17,60] as implemented in the GPUMD package [50].

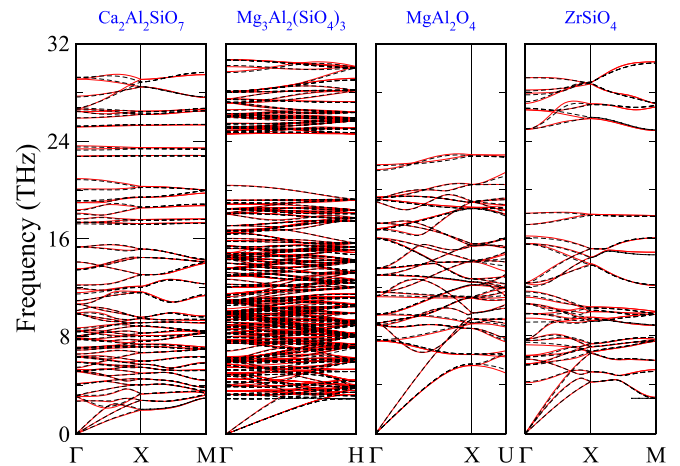


FIG. 1. Phonon dispersion curves along high-symmetry directions of the first Brillouin zone calculated using DFT (solid red lines) and the MTP potentials (dashed black lines).

In the HNEMD method, a slightly nonequilibrium state is created by adding a small external driving force \mathbf{F}_e for the atoms in the simulation box. The heat current generated by this external force is proportional to the thermal conductivity of the system. If the external force is small enough to keep the system in the linear response mode, the relationship between the thermal conductivity and the heat current produced by the external force is [60]

$$\frac{\langle \mathbf{J}(t) \rangle_{ne}}{TV} = \kappa(t) \mathbf{F}_e. \quad (1)$$

If the external force is applied in only one direction, the average value of the thermal conductivity is obtained by integrating the heat flow over the simulation time:

$$\kappa(t) = \frac{1}{t} \int_0^t dt' \frac{\langle \mathbf{J}(t') \rangle_{ne}}{TV \mathbf{F}_e}. \quad (2)$$

C. Comparison of methods for computing thermal conductivity

To analyze our theoretical methods for thermal conductivity, we compare different computational methods and related physics. Specifically, we focus on $\text{La}_2\text{Zr}_2\text{O}_7$, $\text{Mg}_3\text{Al}_2(\text{SiO}_4)_3$, ZrSiO_4 , and BaZrO_3 , and compare results of different methods with experimental data. These materials have been well-studied theoretically and experimentally with reliable results.

Lanthanum zirconate, $\text{La}_2\text{Zr}_2\text{O}_7$ has a cubic pyrochlore-type structure. This material has gained significant attention for TBC applications [61–63] due to its low thermal conductivity, high temperature stability, and chemical inertness. However, accurate prediction of the thermal conductivity of $\text{La}_2\text{Zr}_2\text{O}_7$ remains a challenge due to the complexity of its lattice dynamics and the anharmonic nature of its atomic vibrations [64]. Another good test case is strongly anharmonic pyrope $\text{Mg}_3\text{Al}_2(\text{SiO}_4)_3$ [65–67].

Zirconium silicate (ZrSiO_4) has two known phases stable at different pressures. The low-pressure phase, known as zircon, has a tetragonal body-centered structure with 12 atoms in the unit cell. The crystal structure of zircon comprises an arrangement of SiO_4 tetrahedra and ZrO_8 dodecahedra.

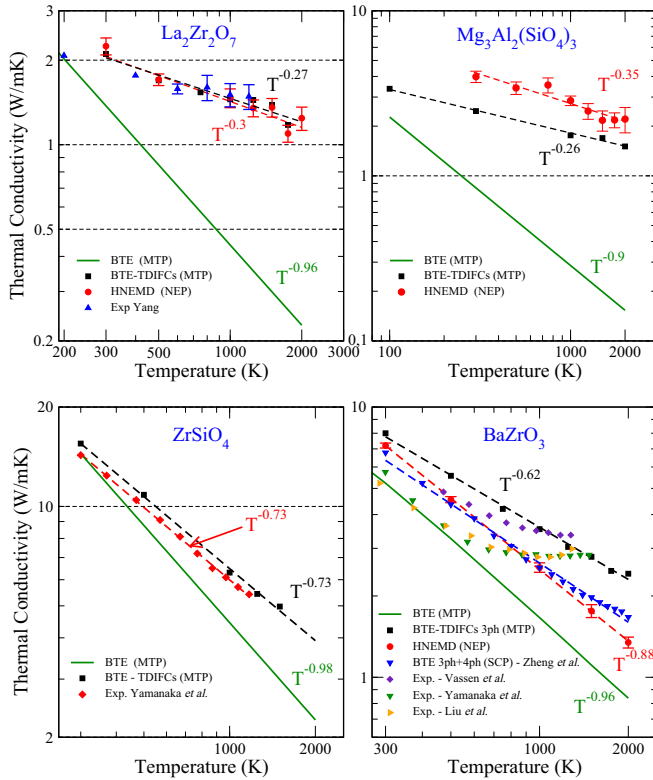


FIG. 2. Calculated thermal conductivity using the BTE (harmonic approximation), EHM (temperature-dependent IFCs), and HNEMD approaches for $\text{La}_2\text{Zr}_2\text{O}_7$, $\text{Mg}_3\text{Al}_2(\text{SiO}_4)_3$ -pyropo, ZrSiO_4 , and BaZrO_3 . The experimental thermal conductivity data for $\text{La}_2\text{Zr}_2\text{O}_7$ are the best measurements for bulk crystal from Ref. [26]. The experimental thermal conductivity data for ZrSiO_4 are from Ref. [71]. For BaZrO_3 the theoretical BTE + SCP calculations from Ref. [72] and experimental results are from Refs. [61,69,70].

Barium zirconate (BaZrO_3) has a simple perovskite structure and was intensely studied due to its promising properties such as high thermal stability and melting point, as well as its dielectric and ferroelectric properties [68]. Recently, BaZrO_3 was explored as a candidate for TBC [61,69,70].

The calculated values of thermal conductivity κ obtained by solving BTE using zero temperature IFCs for all the cases are very close to the available experimental data at low temperatures. (see Fig. 2) As temperature increases, the BTE estimates of $\kappa(T)$ become significantly lower than the experimental values. (The details of solving BTE with zero temperature IFCs are available in Ref. [57].) To uncover the cause of this discrepancy, we compared the phonon scattering rate ($1/\tau$) with their frequency at high temperatures. At $T = 1500$ K, the phonon scattering rate calculated using the conventional BTE method is significantly higher than their frequency (see Fig. SI). It is strange for the scattering rate to exceed the phonon frequency as this indicates that the phonons are decaying before they can even exist, i.e., phonons are not well-defined in this case. This peculiar behavior is also observed in $\text{Mg}_3\text{Al}_2(\text{SiO}_4)_3$ at $T = 1500$ K (see Fig. SI).

Several recent attempts have been made to explain this behavior by considering both the particlelike behavior (kinetic regime in crystals) and the propagation behavior of

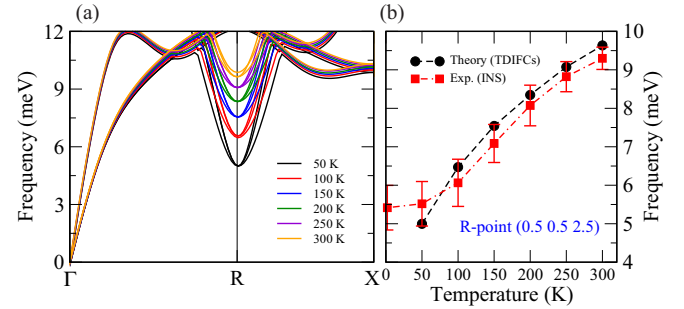


FIG. 3. (a) Phonon dispersion curves of BaZrO_3 calculated using TDIFCs at various temperatures. (b) Comparison of phonon frequencies at the R point (0.5 0.5 2.5) with experimental inelastic neutron scattering from Ref. [76] as a function of temperature. The error bars are estimated based on experimental spectral measurements.

phonons (in glasslike materials) [29,32,73]. Additionally, Wigner transport equation, which offers a unified approach to the coexistence of both particlelike and wavelike mechanisms, has been employed [31,64].

To overcome this problem we decided to use TDIFCs in effective harmonic model [33,34,74] to solve the BTE. To use it, we need to construct a force constants model [74] at each target temperature for each of the materials. For this purpose, we performed molecular dynamics simulations in the canonical ensemble at each temperature in a supercell for 250 ps (the equilibrium lattice constant for each temperature was calculated using the MD simulation in the NPT ensemble for 60 ps). After 40 ps passed for the simulation to reach equilibrium, we selected random snapshots of the molecular dynamics trajectory for training, by least-squares fitting the temperature-dependent interatomic force constants (TDIFCs) [34] in the potential energy surface in the ionic displacements u using the HIPHIVE code [74]:

$$V = V_0 + \Phi_i^\alpha u_i^\alpha + \frac{1}{2} \Phi_{ij}^{\alpha\beta} u_i^\alpha u_j^\beta + \frac{1}{3!} \Phi_{ijk}^{\alpha\beta\gamma} u_i^\alpha u_j^\beta u_k^\gamma + \dots \quad (3)$$

The cutoff values for the second- and third-order interactions were up to 8.0 and 5.0 Å, respectively.

After obtaining the second- and third-order temperature-dependent interatomic force constants using the EHM, we calculated the phonon thermal conductivity using SHENGBTE package (see Fig. 2). Thermal conductivities of $\text{La}_2\text{Zr}_2\text{O}_7$ and ZrSiO_4 obtained using the TDIFCs are in close agreement with experiment. As shown in Fig. 2, the temperature dependence of thermal conductivity $\kappa(T)$ obtained using the TDIFCs significantly differs from that obtained using the zero-temperature IFCs.

The phonon dispersion curves of $\text{La}_2\text{Zr}_2\text{O}_7$ and $\text{Mg}_3\text{Al}_2(\text{SiO}_4)_3$ calculated at 1500 K using the EHM and at 0 K in the harmonic approximation [Figs. SII(b) and SII(d)] show hardening of soft phonons with increasing temperature and shifting toward higher frequencies in both materials. The effect of this hardening is also present in the phonon density of states (PDOS) with increasing temperature [Figs. SII(a) and SII(c)]. The phonon dispersion of BaZrO_3 at different temperatures, obtained using TDIFCs, is presented in Fig. 3(a). A softening in the frequency of the out-of-phase rotation optical mode of oxygen octahedra at the R-point

is observed as the temperature reduction from $T = 300$ to 50 K. To validate our findings, we compared our theoretical results with corresponding experimental measurements of the phonon spectra function obtained via inelastic neutron scattering (INS) for $\text{La}_2\text{Zr}_2\text{O}_7$ [75] (see Fig. SIII) and BaZrO_3 [76] (see Fig. 3) at different temperatures.

The renormalization of phonon frequencies with temperature convinces us to confidently employ TDIFCs in all our future calculations of thermal conductivity for strongly anharmonic materials. In other words, using alternative methods to solve the BTE for these types of materials will not be valid unless those methods incorporate TDIFCs. Here we do not try to use any other approaches, such as the Winger mechanism [64], due to the good agreement between the Boltzmann transport equation, experimental measurements, and HNEMD simulations (which will be discussed below).

The scattering rates of renormalized phonons (Fig. SI) calculated using the TDIFCs are lower than their frequencies, in contrast to the zero-temperature IFCs, indicating normal phonon behavior, rendering phonons well-defined quasiparticles here.

The scattering rate depends on two main parameters, three-phonon scattering phase space [77] and strength of anharmonicity. Our calculation of the three-phonon scattering phase space indicates that the hardening effect reduces the scattering channels for low-frequency phonons (see Ref. [57], Figs. SIV and SV).

Quantitatively measuring anharmonicity in solids is a challenging task as it depends on the thermal expansion of the lattice and the thermal shift of phonon frequencies. Recently, a methodology to calculate the degree of anharmonicity in materials was proposed by Knoop *et al.* [78].

To calculate the degree of anharmonicity, we performed MD simulations at several temperatures using machine learning potentials and calculated harmonic forces using two TDIFCs and zero-temperature IFCs. We performed MD simulations using machine learning potentials at various temperatures and calculated harmonic forces using two TDIFCs and zero-temperature IFCs to determine the degree of anharmonicity. The obtained results for both $\text{La}_2\text{Zr}_2\text{O}_7$ and $\text{Mg}_3\text{Al}_2(\text{SiO}_4)_3$ are presented in Fig. SVI.

In the next step, we ran the MD simulation and used the HNEMD method to calculate thermal conductivity. The NEP3 potential was trained on the same training sets obtained from active learning of the moment tensor potential. The size of simulation box and number of atoms are in Table I. To select the proper value of the external driving force \mathbf{F}_e , we ran several simulations at 300 K with external forces ranging from 10^{-5} to 10^{-4} \AA^{-1} , finally choosing the value of $5 \times 10^{-5} \text{ \AA}^{-1}$. At each temperature, we performed 15 individual simulations and obtained the κ value by averaging the results of each simulation. All the HNEMD simulations were performed for 3 ns in the Nose–Hoover chain thermostat [16,17] to achieve the convergence of the κ value. The results obtained using the EHM and HNEMD, by contrast, show that these methods can be used to calculate the κ values with high accuracy because molecular dynamics takes all anharmonic effects into account.

For $\text{Mg}_3\text{Al}_2(\text{SiO}_4)_3$, the HNEMD-obtained values are higher than those calculated using the EHM, a behavior different from that of $\text{La}_2\text{Zr}_2\text{O}_7$. As a classical method,

molecular dynamics simulation ignores nuclear quantum effects. At temperatures lower than the Debye temperature Θ_D , molecular dynamics will overestimate κ . The Debye temperature of $\text{Mg}_3\text{Al}_2(\text{SiO}_4)_3$ is about 802 K, and the κ values obtained using the HNEMD and EHM at $T > 1000$ K are close to each other. At temperatures above Θ_D , HNEMD yields the most accurate results.

For BaZrO_3 , we compared our results with some experimental measurements [61,69,70] and one theoretical calculation [72] based on self-consistent phonon theory (SCP) in Fig. 2(d). There is a discrepancy between experimental values and obtained values of thermal conductivity using zero temperature IFCs. The thermal conductivity values are in agreement with two measurements by Yamanaka *et al.* [70] and Liu *et al.* [69] only at low temperatures (below $T = 500$ K), and as temperature increases, theory underestimates thermal conductivity. The thermal conductivity values obtained with TDIFCs are, by contrast, significantly higher than those obtained using zero temperature IFCs, particularly at high temperatures ($T > 1000$ K), and exhibit weak agreement with only one experiment conducted by Vassen *et al.* [61] at high temperature.

There is also a discrepancy between HNEMD results and experimental measurements. Notably, the values obtained using HNEMD agree with the experimental measurements by Vassen *et al.* [61] at low temperatures. If we compare our results with other theoretical calculations by Zheng *et al.* [72], which are based on the self-consistent phonon theory, which includes both three- and four-phonon scatterings, we observe a close agreement with our HNEMD results.

The experimental thermal conductivity of BaZrO_3 at high temperatures exhibits a weak temperature dependence that none of the theoretical methods we considered can adequately describe. The temperature dependence obtained using the HNEMD method ($\kappa \propto T^{-0.88}$) is in good agreement with the SCP method ($\kappa \propto T^{-0.75}$) by Zheng *et al.* [72]. However, our calculation based on TDIFCs yields a different temperature dependence of thermal conductivity ($\kappa \propto T^{-0.64}$). These discrepancies may be attributed to other mechanisms of thermal conductivity, such as electronic thermal conductivity, convection with proton [79], oxygen ionic mobility, and thermal radiation, which were not accounted for here.

III. RESULTS AND DISCUSSION

A. Thermal conductivity

Previous section focused on exploring different theoretical approaches for calculating thermal conductivity, along with comparative analyses of experimental measurements for selected compounds. In this section, we extend our investigation by applying the EHM and HNEMD techniques to determine thermal conductivities of both commonly used TBC materials and new materials. Furthermore, we provide a comparison between the theoretically derived thermal conductivities and existing experimental data for some compounds.

Currently, the most widely used material for TBCs is yttria-stabilized zirconia. We calculated the thermal conductivity of 8% YSZ using HNEMD. For this purpose, we employed the NEP4 potential and a supercell of dimensions $8 \times 8 \times 8$

TABLE I. Thermal conductivity and thermal expansion coefficient (TEC) of the compounds calculated using the EHM and HNEMD methods. Compounds are sorted by the thermal conductivity value at $T = 1500$ K. Materials marked with * have anisotropic thermal conductivity.

Compounds (structure)	Thermal conductivity κ , W/(m K)						Volumetric		MD simulation box	
	300 K		1000 K		1500 K		TEC $\times 10^{-5}$ K $^{-1}$		N	
	EHM	HNEMD	EHM	HNEMD	EHM	HNEMD	1000 K	1500 K	Supercell	atoms
MgAl ₂ O ₄ (spinel)	29.21	26.29 \pm 0.60	10.59	6.75 \pm 0.34	7.99	4.58 \pm 0.21	3.47	3.92	8 \times 8 \times 8	28672
ZrSiO ₄ * (zircon)	15.50	16.35 \pm 0.46	6.30	4.60 \pm 0.14	4.98	2.93 \pm 0.16	2.05	2.27	10 \times 10 \times 10	24000
CaAl ₁₂ O ₁₉ * (magnetoplumbite)		4.98 \pm 0.22		3.55 \pm 0.15		2.80 \pm 0.15	3.48	3.76	12 \times 12 \times 3	27648
CaZrAl ₉ BO ₁₈ * (painite)	3.79	5.87 \pm 0.19	1.69	3.08 \pm 0.13	1.27	2.50 \pm 0.12	3.28	3.66	8 \times 8 \times 8	30720
Ca ₃ Al ₂ (SiO ₄) ₃ (garnet)	6.52	6.93 \pm 0.11	2.69	3.12 \pm 0.11	1.91	2.19 \pm 0.11	3.39	3.56	6 \times 6 \times 6	34560
Mg ₃ Al ₂ (SiO ₄) ₃ (garnet)	2.47	3.99 \pm 0.08	1.76	2.85 \pm 0.05	1.69	2.17 \pm 0.08	3.71	3.82	6 \times 6 \times 6	34560
CaYAlO ₄ * (layered perovskite)		4.80 \pm 0.14		2.42 \pm 0.11		2.03 \pm 0.10	4.24	5.10	20 \times 20 \times 6	33600
Y ₃ Al ₅ O ₁₂ (garnet)	4.89	5.58 \pm 0.22	1.90	2.38 \pm 0.10	1.44	2.02 \pm 0.08	3.42	3.70	5 \times 5 \times 5	20000
CaZrTi ₂ O ₇ * (zirconolite)		3.18 \pm 0.13		1.98 \pm 0.13		1.77 \pm 0.16	3.71	4.41	10 \times 10 \times 8	26400
Ca ₂ Al ₂ SiO ₇ * (melilite)	3.63	3.87 \pm 0.08	2.25	2.00 \pm 0.07	1.66	1.77 \pm 0.08	3.39	3.56	9 \times 9 \times 12	23328
BaZrO ₃ (perovskite)	8.00	7.21 \pm 0.15	3.53	2.55 \pm 0.10	2.79	1.76 \pm 0.10	3.18	3.59	18 \times 18 \times 18	29160
SrZrO ₃ (distorted perovskite)		2.93 \pm 0.17		1.87 \pm 0.09		1.64 \pm 0.10	4.10	3.48	18 \times 18 \times 18	29160
CaYAl ₃ O ₇ * (melilite)		1.95 \pm 0.11		1.65 \pm 0.06		1.61 \pm 0.06	3.34	3.38	10 \times 10 \times 14	33600
SrLa ₂ Al ₂ O ₇ * (layered perovskite)		7.98 \pm 0.35		2.74 \pm 0.09		1.56 \pm 0.17	4.57	5.26	16 \times 16 \times 3	18432
Sr ₂ Al ₂ SiO ₇ * (gehlenite type)	4.46	3.93 \pm 0.22	2.09	1.61 \pm 0.10	1.47	1.56 \pm 0.07	3.15	3.25	9 \times 9 \times 12	23328
CaLaAl ₃ O ₇ * (gehlenite type)	3.20	2.47 \pm 0.12	2.01	1.63 \pm 0.05	1.64	1.46 \pm 0.16	3.15	3.25	9 \times 9 \times 12	23328
Sr ₂ CrNbO ₆ (double perovskite)		6.19 \pm 0.26		2.13 \pm 0.19		1.46 \pm 0.11	3.92	4.61	8 \times 8 \times 8	20480
Y ₃ NbO ₇ * (fluorite)		1.61 \pm 0.10		1.26 \pm 0.12		1.41 \pm 0.12	4.62	5.29	8 \times 4 \times 12	16896
Ca ₂ YZr ₂ (AlO ₄) ₃ * (garnet)	3.05	3.56 \pm 0.19	1.37	1.66 \pm 0.15	1.13	1.41 \pm 0.05	3.39	3.66	5 \times 5 \times 5	20000
CaTa ₄ O ₁₁ * (calcioantite)		2.82 \pm 0.13		1.69 \pm 0.10		1.38 \pm 0.07	2.08	2.37	12 \times 12 \times 6	27648
La ₂ Zr ₂ O ₇ (pyrochlore)	2.10	2.24 \pm 0.16	1.45	1.47 \pm 0.11	1.39	1.36 \pm 0.10	3.55	3.57	6 \times 6 \times 6	19008
Ba ₂ YNbO ₆ (double perovskite)		4.14 \pm 0.17		1.76 \pm 0.08		1.36 \pm 0.07	3.58	3.85	8 \times 8 \times 8	20480
Ca ₃ TaAl ₃ Si ₂ O ₁₄ * (langasite)		2.04 \pm 0.15		1.55 \pm 0.12		1.32 \pm 0.15	3.32	3.78	8 \times 8 \times 14	20608
Ba ₂ YTaO ₆ (double perovskite)		4.59 \pm 0.13		1.99 \pm 0.11		1.32 \pm 0.08	3.21	3.50	8 \times 8 \times 8	20480
Y ₄ Al ₂ O ₉ * (cuspidine)	2.86	2.40 \pm 0.09	1.45	1.55 \pm 0.06	1.27	1.30 \pm 0.08	3.02	3.30	8 \times 8 \times 8	30720
BaNd ₂ Ti ₃ O ₁₀ * (layered perovskite)		2.10 \pm 0.15		1.27 \pm 0.15		1.26 \pm 0.10	4.04	4.84	16 \times 8 \times 2	16384
Ba ₃ Ta ₆ (Si ₂ O ₁₃) ₂ * (belkovite)		3.65 \pm 0.13		1.63 \pm 0.09		1.25 \pm 0.08	2.02	2.16	4 \times 8 \times 8	19968
BaLa ₂ Ti ₃ O ₁₀ * (perovskite)		2.30 \pm 0.11		1.51 \pm 0.10		1.24 \pm 0.12	4.51	5.21	16 \times 8 \times 2	16384
Y ₃ TaO ₇ * (distorted weberite)		2.34 \pm 0.10		1.37 \pm 0.08		1.18 \pm 0.09	4.47	4.58	8 \times 4 \times 12	16896
Ba ₃ Nb ₆ (Si ₂ O ₁₃) ₂ * (belkovite)		2.39 \pm 0.15		1.37 \pm 0.12		1.14 \pm 0.08	2.47	2.75	4 \times 8 \times 8	19968
BaLaMgNbO ₆ (double perovskite)		2.24 \pm 0.10		1.34 \pm 0.11		1.14 \pm 0.09	4.81	5.40	8 \times 8 \times 8	20480
Ca ₃ ZrSi ₂ O ₉ * (cuspidine)	2.49	2.07 \pm 0.16	1.48	1.14 \pm 0.08	1.30	1.12 \pm 0.11	3.55	4.04	10 \times 8 \times 8	38400
Ba ₆ Ti ₂ Nb ₈ O ₃₀ * (tetragonal tungsten bronze)		1.92 \pm 0.11		1.25 \pm 0.11		1.12 \pm 0.10	3.76	5.43	5 \times 5 \times 16	18400
Sr ₃ LaTa ₃ O ₁₂ * (layered perovskite)		2.41 \pm 0.13		1.17 \pm 0.11		1.10 \pm 0.10	4.59	4.87	6 \times 10 \times 2	13680
BaLaMgTaO ₆ (double perovskite)		2.28 \pm 0.11		1.22 \pm 0.12		1.11 \pm 0.10	4.64	5.16	8 \times 8 \times 8	20480
Y ₄ Ca(SiO ₄) ₃ O* (apatite)		2.03 \pm 0.10		1.28 \pm 0.10		1.04 \pm 0.05	3.52	4.02	8 \times 8 \times 10	26880
Ba ₃ LaTa ₃ O ₁₂ * (layered perovskite)		2.19 \pm 0.17		1.19 \pm 0.09		0.84 \pm 0.09	3.09	3.10	6 \times 10 \times 2	13680
8% YSZ (distorted fluorite)		2.24 \pm 0.13		1.64 \pm 0.08		--	4.06	5.02	8 \times 8 \times 8	40448

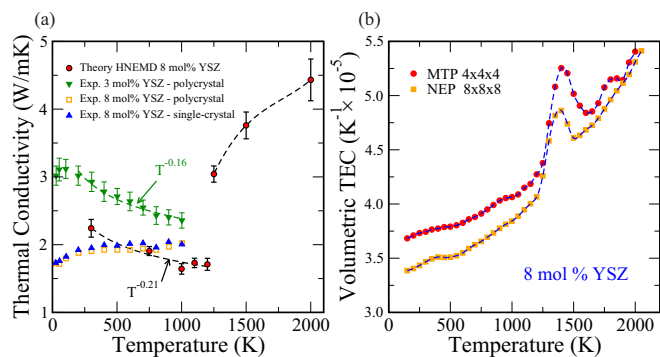


FIG. 4. (a) Comparison between the thermal conductivity of 8% YSZ obtained using HNEMD and experimental data from Ref. [80]. The experimental data correspond to 8% YSZ single-crystal and polycrystal samples, as well as 3% YSZ polycrystal samples. (b) The temperature-dependent volumetric thermal expansion coefficient of 8% YSZ, obtained through molecular dynamics simulations employing two machine learning potentials: MTP and NEP. The peak observed at 1400 K corresponds to a phase transition.

containing 40448 atoms. The driving force for the simulations was set to $5 \times 10^{-5} \text{ \AA}^{-1}$. The HNEMD results, along with the comparison to experimental data via Schlichting *et al.* [80] for 8% YSZ single-crystal and polycrystal samples, as well as 3% YSZ polycrystal samples, are presented in the Fig. 4(a).

The HNEMD thermal conductivity for 8% YSZ in two separate sections for temperatures $T < 1250$ and > 1250 K are presented in Fig. 4(a). The temperature dependence of thermal conductivity at temperatures less than 1250 K for both single-crystal and polycrystalline samples is nearly zero, and the temperature dependence obtained from HNEMD is also very small ($\kappa \propto T^{-0.21}$). We found that phonons are the dominant heat carriers at temperatures below 1200 K, and due to the strongly anharmonic interatomic potential and the complex structure of 8% YSZ, the dependence of thermal conductivity on temperature is also very small. However, with increasing temperature and with phase transition in YSZ around 1400 K, due to diffusion of oxygen atoms [81], the convective heat transport becomes significant, and the thermal conductivity sharply increase.

Using the EHM, we calculated the thermal conductivity at high temperatures for other candidate materials for TBC (Fig. 5, Table I). The results obtained using the TDIFCs show the temperature dependence of the thermal conductivity $\kappa \propto T^{-\alpha}$, where $\alpha \leq 1$ and is specific for each compound. Overall, materials having a low thermal conductivity at room temperature show small temperature dependence of κ at higher temperatures.

Using the HNEMD approach and machine-learning neuroevolution potentials, we calculated the thermal conductivity of all candidate TBC materials at 300, 1000, and 1500 K, see Fig. 6 and Table I. To compare these theoretical results with experimental measurements, we have tabulated them in Table II and represented them graphically in Fig. 7. An important observation from Fig. 7 is that our theoretical approach (HNEMD) tends to overestimate the thermal conductivity at low temperatures, while underestimating it at high temperatures. This discrepancy can be attributed to the classical nature of the MD simulation employed, which leads to an

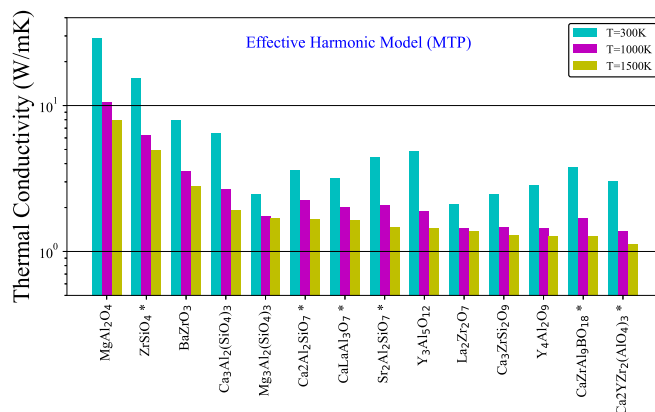


FIG. 5. Thermal conductivity of some materials calculated using the effective harmonic method and machine-learning moment tensor potential. The compounds are sorted by the value of thermal conductivity at $T = 1500$ K. (Materials marked with * have anisotropic thermal conductivity.)

overestimation of heat capacity at low temperatures and, consequently, higher thermal conductivity within that temperature range. At high temperatures, there could be multiple thermal conductance mechanisms or heat carriers, whereas we have only considered the phononic heat transport in our analysis. Additionally, overestimation of thermal expansion in MD simulations may lead to underestimation of thermal conductivity of high temperatures which will be further discussed below.

By taking into account the predictive errors in thermal conductivity using both EHM and HNEMD with machine learning potentials, it can be asserted that our approach in structurally complex and strongly anharmonic systems is faster than AIMD, and more accurate than classical potentials. Integrating this methodology with other techniques, such as measuring the degree of anharmonicity, holds potential for significant advancements in high-throughput screening of thermal conductivity of materials.

B. Thermal expansion coefficient

Low thermal conductivity is not the only requirement for TBC materials. The thermal expansion coefficient of a TBC material must be as close as possible to the substrate to ensure the stability of the coating.

To calculate the thermal expansion coefficient, we used the MD simulation with ML potentials, using the LAMMPS package. The quasiharmonic approximation (QHA) is another way to calculate the TEC which it is very accurate below the Debye temperature because it takes into account the quantum statistics of phonons, but becomes less accurate at high temperatures where higher-order anharmonic effects (the so-called intrinsic anharmonic effects, which are neglected within the QHA) become important. On the other hand, MD simulations fully include anharmonicity and are more accurate than QHA at high temperatures. The calculated values of the volumetric TEC using MD at $T = 1000$ and 1500 K are presented in Table I.

Comparing the calculated thermal expansion values with MD using machine learning potentials and the experimentally measured values at different temperatures provides valuable

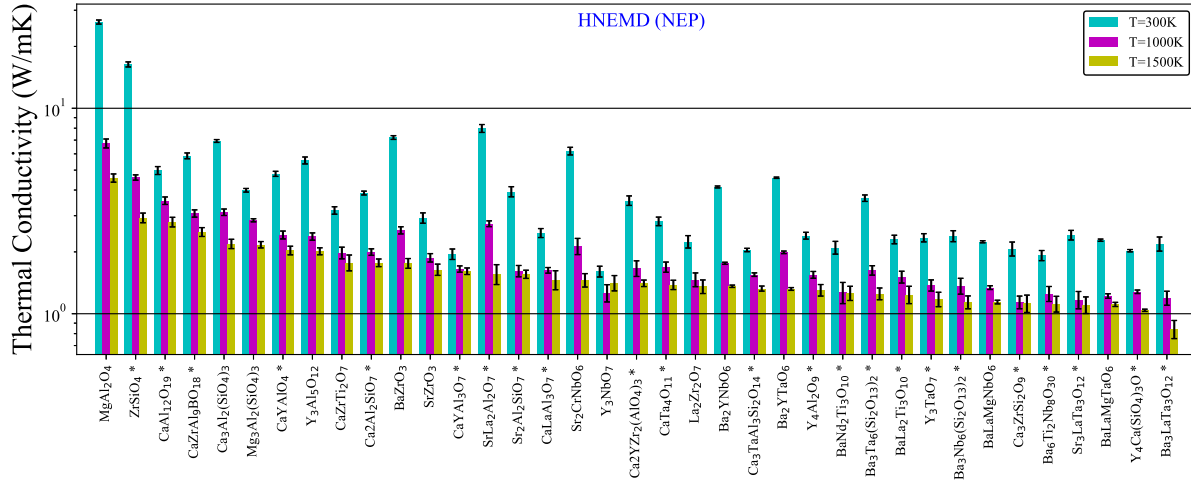


FIG. 6. Thermal conductivity of the materials calculated using the HNEMD and machine-learning neuroevolution potential. The compounds are sorted by the value of thermal conductivity at $T = 1500$ K. Materials marked with * have anisotropic thermal conductivity.

insights into the accuracy of the theoretical approach employed. As clearly shown in Fig. 8, the predicted thermal expansion values using MD are higher than the experimentally measured values. This is typical of the GGA approximation of DFT - and our machine learning interatomic potentials were trained on GGA data.

C. Elastic constants and mechanical properties

Mechanical properties, such as strength, and hardness are important for TBC materials because they affect the coating’s ability to withstand the thermal and mechanical stresses that it experiences in service. The TBC must be able to withstand the thermal gradients and thermal cycling that occur during operation, as well as any mechanical loads that may be applied. If a TBC does not have adequate mechanical properties,

it may crack or fail prematurely, which can lead to component failure. Additionally, good mechanical properties are important for TBCs in order to maintain good adhesion between the TBC and the substrate, and to prevent spallation.

In the homogeneous deformation of a crystal, the relationship between strain and stress can be written as [117]

$$\sigma_{ij} = C_{ijkl}\epsilon_{kl} \tag{4}$$

where σ_{ij} and ϵ_{kl} are the stress and strain tensors, respectively, and C_{ijkl} is the elastic stiffness tensor. For easier calculation, the stress-strain relationship can be expressed using the strain energy density function U through the work conjugate relation [118]:

$$\sigma_{ij} = \frac{\partial U}{\partial \epsilon_{ij}}. \tag{5}$$

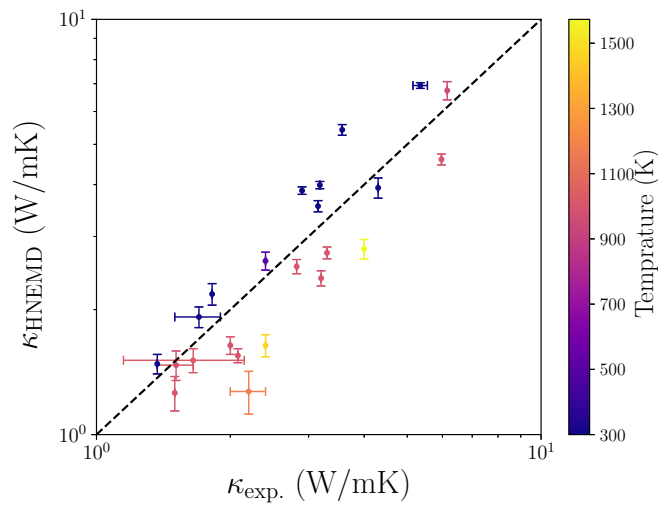


FIG. 7. Correlation between theoretical calculated thermal conductivity using HNEMD and available experimental data on some TBC materials at different temperatures $T = 300$ to 1473 K. (The references of experimental data are available in Table II.)

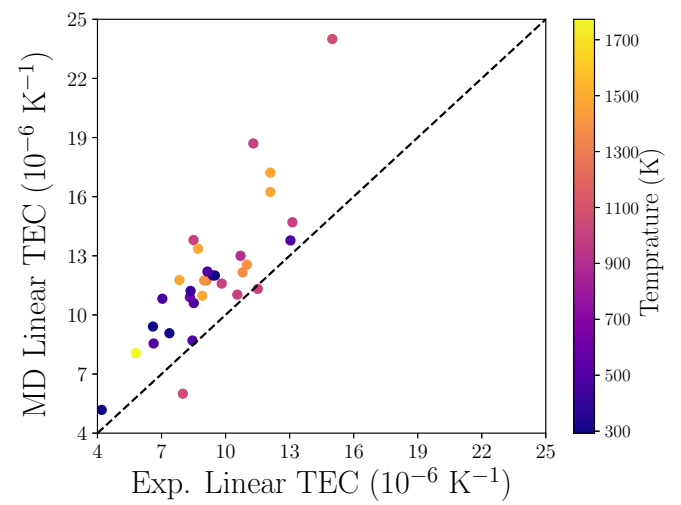


FIG. 8. Correlation between the linear thermal expansion calculated using MD and experimental data at different temperatures from $T = 300$ to 1473 K. (The references of experimental data are available in Table II.)

TABLE II. Comparison of the calculated thermal conductivity and thermal expansion coefficient of compounds with available experimental data. Materials marked with * have anisotropic thermal conductivity. For our theoretical data, the temperatures are the same as for experimental data.

Compound (structure)	Thermal conductivity κ , W/(m K)		Linear TEC $\times 10^{-6}$ K $^{-1}$	
	Experiment	This work HNEMD	Experiment	This work MD
MgAl ₂ O ₄ (spinel) [82–84]	6.15 (955 K)	6.75 \pm 0.34	9.82 (1003 K)	11.59
ZrSiO ₄ * (zircon) [71,85]	5.97 (1000 K)	4.60 \pm 0.14	4.2-5.8 (up to 1773 K)	5.18-8.06
CaAl ₁₂ O ₁₉ * (magnetoplumbite) [86,87]	~4 (1573 K)	2.80 \pm 0.15	7.3 (a) 11.8 (c)	6.8
Ca ₃ Al ₂ (SiO ₄) ₃ (garnet) [88,89]	5.1-5.6 (300 K)	6.93 \pm 0.11	9 (1400 K)	11.75
Mg ₃ Al ₂ (SiO ₄) ₃ (garnet) [88,89]	3.18 (300 K)	3.99 \pm 0.08	10 (1400 K)	12.55
CaYAlO ₄ * (layered perovskite) [90–92]	3.57 (a) (300 K)	5.42 \pm 0.16	8-11 (a) (up to 1200 K)	6
	3.15 (c) (300 K)	3.55 \pm 0.11	11-15 (c) (up to 1200 K)	24
Y ₃ Al ₅ O ₁₂ (garnet) [93,94]	3.2 (1000 K)	2.38 \pm 0.10	8.33 (600 K) 13.13 (a) (1000 K)	10.9 14.70 (a)
CaZrTi ₂ O ₇ * (zirconolite) [95,96] ^a	2.09 (300 K)	3.18 \pm 0.13	10.55 (b) (1000 K) 11.51 (c) (1000 K)	11.03 (b) 11.32 (c)
Ca ₂ Al ₂ SiO ₇ * (melilite) [97,98]	2.9 (300 K)	3.87 \pm 0.08	8.45 (a) (500 K) 13.04 (c) (500 K)	8.70 (a) 13.78 (c)
BaZrO ₃ (perovskite type) [69,70]	2.82 (1000 K)	2.55 \pm 0.10	7.84 (1473 K)	11.77
SrZrO ₃ (distorted perovskite) [99] ^a	2.4 (1473 K)	1.64 \pm 0.10	10.8 (1373 K)	12.16
CaYAl ₃ O ₇ * (melilite) [100]	1.82 (a) (300 K)	2.18 \pm 0.13	6.63 (a)	8.55 (a)
	1.37 (c) (300 K)	1.48 \pm 0.08	28.52 (c)	11.21 (c)
SrLa ₂ Al ₂ O ₇ * (layered perovskite) [101,102]	3.3 (1000 K)	2.74 \pm 0.09	8.5 (a) (1273 K), theory 11.3 (c) (1273 K), theory	13.8 (a) 18.7 (c)
Sr ₂ Al ₂ SiO ₇ * (melilite) [97]	4.3 (300 K)	3.93 \pm 0.22	–	–
Y ₃ NbO ₇ * (fluorite type) [103,104]	~1.5 (1273 K)	1.26 \pm 0.12	10.35 (325-1023 K)	~13.4
La ₂ Zr ₂ O ₇ (pyrochlore type) [26,61]	1.51 \pm 0.14 (1000 K)	1.47 \pm 0.11	9.1 (1273 K)	11.75
Ba ₂ YNbO ₆ (double perovskite) [105]	–	–	8.36 (400-1000 K)	11.22
Ca ₃ TaAl ₃ Si ₂ O ₁₄ * (langasite type) [106]	–	–	~8.51 (a) (300-1473 K) ~9.15 (c) (300-1473 K)	~10.6 (a) ~12.2 (c)
Ba ₂ YTaO ₆ (double perovskite) [107]	–	–	6.6 (300 K)	9.41
Y ₄ Al ₂ O ₉ * (cuspidine) [108,109] ^a	2.08 (1000 K)	1.55 \pm 0.06	7.37-8.91 (300-1473 K)	9.07-10.97
BaNd ₂ Ti ₃ O ₁₀ * (layered perovskite) [110,111]	2.0-2.4 (1173 K)	1.27 \pm 0.15	~9.4-12.1 (473-1473 K)	~12-16.24
BaLa ₂ Ti ₃ O ₁₀ * (layered perovskite) [112]	1.60-1.71 (1023 K)	1.51 \pm 0.10	~9.5-12.1 (293-1473 K)	~12.42-17.22
Ca ₃ ZrSi ₂ O ₉ * (baghdadite) [113]	–	–	7.04-8.71 (473-1473 K, film)	10.82-13.36
Ba ₆ Ti ₂ Nb ₈ O ₃₀ * (tetragonal tungsten bronze) [114]	1.7 \pm 0.2 (300 K)	1.92 \pm 0.11	–	–
Y ₄ Ca(SiO ₄) ₃ O* (apatite) [115]	1.7 (300 K) ^b	2.03 \pm 0.10	7.1 (a) (300 K) ^b 5.7 (c) (300 K) ^b	11.06 (a) 10.10 (c)
8% YSZ (distorted fluorite type) [80,116]	2.0 (1000 K)	1.64 \pm 0.08	10.7 (293-1273 K)	~13

^aThere are phase transitions.

^bRefer to the crystal composition (Y_{2.28}Er_{1.5}Tm_{0.15}Ho_{0.1})Ca(SiO₄)₃O.

From Eq. 4, it follows that

$$C_{ijkl} = \frac{\partial \sigma_{ij}}{\partial \epsilon_{kl}}. \quad (6)$$

We employed the Voigt-Reuss-Hill [119–121] averaging scheme to obtain the effective elastic moduli. The speed of sound (elastic waves) in crystals can be calculated using the bulk modulus K , shear modulus G , and mass

density ρ :

$$v_l = \sqrt{\frac{3K + 4G}{3\rho}}, \quad v_t = \sqrt{\frac{G}{\rho}}, \quad (7)$$

$$v_m = \left[\frac{1}{3} \left(\frac{2}{v_t^3} + \frac{1}{v_l^3} \right) \right]^{-1/3} \quad (8)$$

where v_l , v_t , and v_m are the longitudinal, transverse, and average speeds of sound, respectively.

At temperatures below Debye temperature (Θ_D), acoustic phonons play a particularly important role in determining the

TABLE III. Comparison of the elastic constants C_{ij} , bulk modulus K , and shear modulus G calculated using the DFT and MTP and measured in the experiment.

Compounds	Method	Elastic properties, GPa				
		C_{11}	C_{12}	C_{44}	K	G
$\text{La}_2\text{Zr}_2\text{O}_7$	DFT	265.07	104.36	85.25	157.93	83.89
	MTP	264.37	104.42	85.12	157.74	83.03
	Exp. [122]				157.00	
SrZrO_3	DFT	318.22	71.73	74.98	153.90	91.60
	MTP	307.50	75.15	71.76	152.60	87.12
	Exp. [123]				150.00	
$\text{Mg}_3\text{Al}_2(\text{SiO}_4)_3$	DFT	271.73	102.26	82.09	158.75	83.14
	MTP	284.13	101.60	92.87	162.44	92.22
	Exp. [124]				171.40	93

heat capacity and thermal conductivity. To calculate Θ_D , we used the expression

$$\Theta_D = \frac{h}{k_B} \left(\frac{3q N \rho}{4\pi M} \right)^{1/3} v_m, \quad (9)$$

where v_m is the average speed of sound, k_B is the Boltzmann constant, N is the Avogadro number, h is the Planck constant, q is the total number of atoms in the cell, M is the molecular weight, and ρ is the density.

To calculate the elastic constants from the strain-energy relationship, we utilized the elastic_vasp package [125,126] interfaced with VASP and MLIP. We used MTP potentials to determine the elastic constants and compared our findings to DFT and experimental data for three compounds in Table III. Close agreement with experiment is observed for both the DFT- and MTP-obtained values of the bulk modulus K .

We investigated the relationship of the thermal conductivity with such properties as Young's modulus, Debye temperature, and speed of sound (Fig. 9). Materials with thermal conductivity below 2 W/(m K) at temperatures above 1000 K have Young's modulus smaller than 250 GPa and the Debye temperature under 600 K. These values can be used as a threshold for choosing materials with low thermal conductivity for future high-throughput studies.

IV. SOME PRACTICAL ASPECTS

Based on our calculations of the key physical properties (thermal conductivity, thermal expansion, and elastic constants) of complex oxides selected in this work, we can draw practical conclusions about them as possible candidates for TBCs. Within the temperature range of 1000 to 1500 K, we have set a threshold for thermal conductivity of 2 W/(m K) and a range of $(3.0\text{--}5.0) \times 10^{-5} \text{ K}^{-1}$ for volumetric TEC in our materials selection process for TBC applications. By applying these criteria, we have chosen 23 compounds (highlighted by the blue rectangle in Fig. 10). Among these compounds, some are already used as TBCs, while others, such as $\text{Sr}_3\text{LaTa}_3\text{O}_{12}$, $\text{Ba}_3\text{LaTa}_3\text{O}_{12}$, $\text{Ba}_6\text{Ti}_2\text{Nb}_8\text{O}_{30}$, Ba_2YNbO_6 , Ba_2YTao_6 , BaLaMgNbO_6 , BaLaMgTaO_6 , $\text{Y}_4\text{Ca}(\text{SiO}_4)_3\text{O}$,

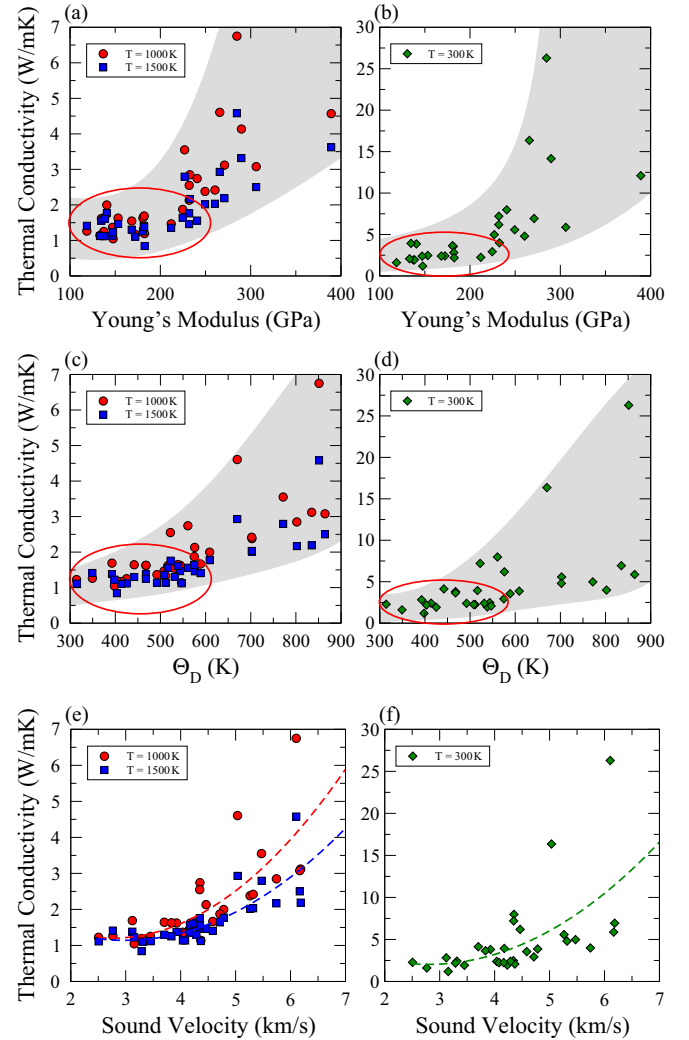


FIG. 9. Thermal conductivity of candidate materials plotted against [(a) and (b)] Young's modulus, [(c) and (d)] Debye temperature, and [(e) and (f)] sound velocity at $T = 300, 1000,$ and 1500 K .

$\text{Ca}_2\text{YZr}_2(\text{AlO}_4)_3$, and $\text{CaLaAl}_3\text{O}_7$, have not been previously studied experimentally or theoretically as TBCs.

The materials used in TBCs should possess not only low thermal conductivity but also mechanical stability under harsh conditions and high temperatures, enduring various stresses caused by thermal cycling. The coating must be able to tolerate the expansion and contraction of the underlying substrate without cracking or delaminating. When evaluating materials for TBCs, parameters such as quasiductility should be considered. This can be done using Pugh's ratio defined as the ratio of the shear modulus to the bulk modulus (G/K ratio), and serving as a good measure of quasiductility [127,128]. An appropriate threshold for selecting suitable materials for TBCs is Pugh's ratio less than 0.57. The bulk and shear moduli for the selected materials in the previous section are presented in Table IV. All chosen materials have Pugh's ratio below 0.57 and are suitable for use in TBCs.

Besides the above physical properties, chemical and other aspects should be taken into account to choose suitable

- [1] L. L. Huang, H. M. Meng, J. Tang, S. Li, and Z. Q. Yu, Overview on double ceramic layer thermal barrier coatings, *Adv. Mater. Res.* **1053**, 364 (2014).
- [2] R. Vaßen, E. Bakan, D. E. Mack, and O. Guillon, A perspective on thermally sprayed thermal barrier coatings: Current status and trends, *J. Therm. Spray Tech.* **31**, 685 (2022).
- [3] B. Liu, Y. Liu, C. Zhu, H. Xiang, H. Chen, L. Sun, Y. Gao, and Y. Zhou, Advances on strategies for searching for next generation thermal barrier coating materials, *J. Mater. Sci. Technol.* **35**, 833 (2019).
- [4] S. Ghosh, Thermal barrier ceramic coatings—a review, in *Advanced Ceramic Processing* (In Tech, London, UK, 2015), pp. 111–138.
- [5] S. M. Lakiza, M. I. Grechanyuk, O. K. Ruban, V. P. Redko, M. S. Glabay, O. B. Myloserdov, O. V. Dudnik, and S. V. Prokhorenko, Thermal barrier coatings: Current status, search, and analysis, *Powder Metall. Met. Ceram.* **57**, 82 (2018).
- [6] A. van Rookeghem, J. Carrete, C. Oses, S. Curtarolo, and N. Mingo, High-throughput computation of thermal conductivity of high-temperature solid phases: The case of oxide and fluoride perovskites, *Phys. Rev. X* **6**, 041061 (2016).
- [7] A. Tewari, S. Dixit, N. Sahni, and S. P. Bordas, Machine learning approaches to identify and design low thermal conductivity oxides for thermoelectric applications, *Data-Centric Eng.* **1**, e8 (2020).
- [8] A. Seko, A. Togo, H. Hayashi, K. Tsuda, L. Chaput, and I. Tanaka, Prediction of low-thermal-conductivity compounds with first-principles anharmonic lattice-dynamics calculations and bayesian optimization, *Phys. Rev. Lett.* **115**, 205901 (2015).
- [9] L. Chen, H. Tran, R. Batra, C. Kim, and R. Ramprasad, Machine learning models for the lattice thermal conductivity prediction of inorganic materials, *Comput. Mater. Sci.* **170**, 109155 (2019).
- [10] H. Babaei, R. Guo, A. Hashemi, and S. Lee, Machine-learning-based interatomic potential for phonon transport in perfect crystalline Si and crystalline Si with vacancies, *Phys. Rev. Mater.* **3**, 074603 (2019).
- [11] W. G. Hoover and W. T. Ashurst, Nonequilibrium molecular dynamics, *Theor. Chem. Adv. Perspect.* **1**, 1 (1975).
- [12] T. Ikeshoji and B. Hafskjold, Non-equilibrium molecular dynamics calculation of heat conduction in liquid and through liquid-gas interface, *Mol. Phys.* **81**, 251 (1994).
- [13] P. Jund and R. Jullien, Molecular-dynamics calculation of the thermal conductivity of vitreous silica, *Phys. Rev. B* **59**, 13707 (1999).
- [14] M. S. Green, Markoff random processes and the statistical mechanics of time-dependent phenomena. II. Irreversible processes in fluids, *J. Chem. Phys.* **22**, 398 (1954).
- [15] R. Kubo, M. Yokota, and S. Nakajima, Statistical-mechanical theory of irreversible processes. II. Response to thermal disturbance, *J. Phys. Soc. Jpn.* **12**, 1203 (1957).
- [16] D. J. Evans, Homogeneous NEMD algorithm for thermal conductivity—Application of non-canonical linear response theory, *Phys. Lett. A* **91**, 457 (1982).
- [17] D. J. Evans and B. L. Holian, The Nose–Hoover thermostat, *J. Chem. Phys.* **83**, 4069 (1985).
- [18] R. Peierls, On the kinetic theory of thermal conduction in crystals, *Ann. Phys.* **395**, 1055 (1929).
- [19] M. Omini and A. Sparavigna, An iterative approach to the phonon Boltzmann equation in the theory of thermal conductivity, *Phys. B: Condens. Matter* **212**, 101 (1995).
- [20] M. Omini and A. Sparavigna, Beyond the isotropic-model approximation in the theory of thermal conductivity, *Phys. Rev. B* **53**, 9064 (1996).
- [21] J. S. Wang, J. Wang, and J. T. Lü, Quantum thermal transport in nanostructures, *Eur. Phys. J. B* **62**, 381 (2008).
- [22] D. R. Clarke, Materials selection guidelines for low thermal conductivity thermal barrier coatings, *Surf. Coat. Technol.* **163-164**, 67 (2003).
- [23] D. T. Morelli, J. P. Heremans, and G. A. Slack, Estimation of the isotope effect on the lattice thermal conductivity of group IV and group III-V semiconductors, *Phys. Rev. B* **66**, 195304 (2002).
- [24] T. Fan and A. R. Oganov, AICON2: A program for calculating transport properties quickly and accurately, *Comput. Phys. Commun.* **266**, 108027 (2021).
- [25] G. Slack, Nonmetallic crystals with high thermal conductivity, *J. Phys. Chem. Solids* **34**, 321 (1973).
- [26] J. Yang, C. Wan, M. Zhao, M. Shahid, and W. Pan, Effective blocking of radiative thermal conductivity in $\text{La}_2\text{Zr}_2\text{O}_7/\text{LaPO}_4$ composites for high temperature thermal insulation applications, *J. Eur. Ceram. Soc.* **36**, 3809 (2016).
- [27] L. Chen, M. Hu, J. Guo, X. Chong, and J. Feng, Mechanical and thermal properties of RETaO_4 (RE = Yb, Lu, Sc) ceramics with monoclinic-prime phase, *J. Mater. Sci. Technol.* **52**, 20 (2020).
- [28] Z. Tian, L. Zheng, J. Wang, P. Wan, J. Li, and J. Wang, Theoretical and experimental determination of the major thermo-mechanical properties of RE_2SiO_5 (RE = Tb, Dy, Ho, Er, Tm, Yb, Lu, and Y) for environmental and thermal barrier coating applications, *J. Eur. Ceram. Soc.* **36**, 189 (2016).
- [29] S. Mukhopadhyay, D. S. Parker, B. C. Sales, A. A. Puretzky, M. A. McGuire, and L. Lindsay, Two-channel model for ultralow thermal conductivity of crystalline Tl_3VSe_4 , *Science* **360**, 1455 (2018).
- [30] L. Isaeva, G. Barbalinardo, D. Donadio, and S. Baroni, Modeling heat transport in crystals and glasses from a unified lattice-dynamical approach, *Nat. Commun.* **10**, 3853 (2019).
- [31] M. Simoncelli, N. Marzari, and F. Mauri, Unified theory of thermal transport in crystals and glasses, *Nat. Phys.* **15**, 809 (2019).
- [32] Y. Luo, X. Yang, T. Feng, J. Wang, and X. Ruan, Vibrational hierarchy leads to dual-phonon transport in low thermal conductivity crystals, *Nat. Commun.* **11**, 2554 (2020).
- [33] P. Souvatzis, O. Eriksson, M. I. Katsnelson, and S. P. Rudin, Entropy driven stabilization of energetically unstable crystal structures explained from first principles theory, *Phys. Rev. Lett.* **100**, 095901 (2008).
- [34] O. Hellman, I. A. Abrikosov, and S. I. Simak, Lattice dynamics of anharmonic solids from first principles, *Phys. Rev. B* **84**, 180301(R) (2011).
- [35] K. Esfarjani and H. T. Stokes, Method to extract anharmonic force constants from first principles calculations, *Phys. Rev. B* **77**, 144112 (2008).
- [36] W. Li, J. Carrete, N. Katcho, and N. Mingo, ShengBTE: A solver of the Boltzmann transport equation for phonons, *Comput. Phys. Commun.* **185**, 1747 (2014).

- [37] J. Behler, Perspective: Machine learning potentials for atomistic simulations, *J. Chem. Phys.* **145**, 170901 (2016).
- [38] J. Behler and M. Parrinello, Generalized neural-network representation of high-dimensional potential-energy surfaces, *Phys. Rev. Lett.* **98**, 146401 (2007).
- [39] A. P. Bartók, J. Kermode, N. Bernstein, and G. Csányi, Machine learning a general-purpose interatomic potential for silicon, *Phys. Rev. X* **8**, 041048 (2018).
- [40] B. Cheng, E. A. Engel, J. Behler, C. Dellago, and M. Ceriotti, Ab initio thermodynamics of liquid and solid water, *Proc. Natl. Acad. Sci. USA* **116**, 1110 (2019).
- [41] X. Qian and R. Yang, Temperature effect on the phonon dispersion stability of zirconium by machine learning driven atomistic simulations, *Phys. Rev. B* **98**, 224108 (2018).
- [42] A. V. Shapeev, Moment tensor potentials: A class of systematically improvable interatomic potentials, *Multiscale Model. Simul.* **14**, 1153 (2016).
- [43] E. V. Podryabinkin and A. V. Shapeev, Active learning of linearly parametrized interatomic potentials, *Comput. Mater. Sci.* **140**, 171 (2017).
- [44] K. Gubaev, E. V. Podryabinkin, G. L. Hart, and A. V. Shapeev, Accelerating high-throughput searches for new alloys with active learning of interatomic potentials, *Comput. Mater. Sci.* **156**, 148 (2019).
- [45] Y. Zuo, C. Chen, X. Li, Z. Deng, Y. Chen, J. Behler, G. Csányi, A. V. Shapeev, A. P. Thompson, M. A. Wood, and S. P. Ong, Performance and cost assessment of machine learning interatomic potentials, *J. Phys. Chem. A* **124**, 731 (2020).
- [46] I. S. Novikov, K. Gubaev, E. V. Podryabinkin, and A. V. Shapeev, The MLIP package: moment tensor potentials with MPI and active learning, *Mach. Learn.: Sci. Technol.* **2**, 025002 (2021).
- [47] Z. Fan, Z. Zeng, C. Zhang, Y. Wang, K. Song, H. Dong, Y. Chen, and T. Ala-Nissila, Neuroevolution machine learning potentials: Combining high accuracy and low cost in atomistic simulations and application to heat transport, *Phys. Rev. B* **104**, 104309 (2021).
- [48] Z. Fan, Improving the accuracy of the neuroevolution machine learning potential for multi-component systems, *J. Phys.: Condens. Matter* **34**, 125902 (2022).
- [49] Z. Fan, Y. Wang, P. Ying, K. Song, J. Wang, Y. Wang, Z. Zeng, K. Xu, E. Lindgren, J. M. Rahm, A. J. Gabourie, J. Liu, H. Dong, J. Wu, Y. Chen, Z. Zhong, J. Sun, P. Erhart, Y. Su, and T. Ala-Nissila, GPUMD: A package for constructing accurate machine-learned potentials and performing highly efficient atomistic simulations, *J. Chem. Phys.* **157**, 114801 (2022).
- [50] Z. Fan, W. Chen, V. Vierimaa, and A. Harju, Efficient molecular dynamics simulations with many-body potentials on graphics processing units, *Comput. Phys. Commun.* **218**, 10 (2017).
- [51] G. Kresse and J. Furthmüller, Efficient iterative schemes for ab initio total-energy calculations using a plane-wave basis set, *Phys. Rev. B* **54**, 11169 (1996).
- [52] P. E. Blöchl, Projector augmented-wave method, *Phys. Rev. B* **50**, 17953 (1994).
- [53] J. P. Perdew, K. Burke, and M. Ernzerhof, Generalized gradient approximation made simple, *Phys. Rev. Lett.* **77**, 3865 (1996).
- [54] H. J. Monkhorst and J. D. Pack, Special points for brillouin-zone integrations, *Phys. Rev. B* **13**, 5188 (1976).
- [55] M. Parrinello and A. Rahman, Crystal structure and pair potentials: A molecular-dynamics study, *Phys. Rev. Lett.* **45**, 1196 (1980).
- [56] M. Parrinello and A. Rahman, Polymorphic transitions in single crystals: A new molecular dynamics method, *J. Appl. Phys.* **52**, 7182 (1981).
- [57] See Supplemental Material at <http://link.aps.org/supplemental/10.1103/PhysRevMaterials.8.033601> for details on different quantities (weighted phase space of three-phonon scattering, supercell size, k-points, number of atoms in supercell used for training ML potentials, errors for each type of ML potential, supercell size for extracting the second- and third-order interatomic force constants (IFCs), and q-grid to solve the Boltzmann transport equation).
- [58] A. P. Thompson, H. M. Aktulga, R. Berger, D. S. Bolintineanu, W. M. Brown, P. S. Crozier, P. J. in 't Veld, A. Kohlmeyer, S. G. Moore, T. D. Nguyen, R. Shan, M. J. Stevens, J. Tranchida, C. Trott, and S. J. Plimpton, LAMMPS - a flexible simulation tool for particle-based materials modeling at the atomic, meso, and continuum scales, *Comput. Phys. Commun.* **271**, 108171 (2022).
- [59] A. Togo, F. Oba, and I. Tanaka, First-principles calculations of the ferroelastic transition between rutile-type and CaCl₂-type SiO₂ at high pressures, *Phys. Rev. B* **78**, 134106 (2008).
- [60] Z. Fan, H. Dong, A. Harju, and T. Ala-Nissila, Homogeneous nonequilibrium molecular dynamics method for heat transport and spectral decomposition with many-body potentials, *Phys. Rev. B* **99**, 064308 (2019).
- [61] R. Vassen, X. Cao, F. Tietz, D. Basu, and D. Stöver, Zirconates as new materials for thermal barrier coatings, *J. Am. Ceram. Soc.* **83**, 2023 (2000).
- [62] B. Saruhan, P. Francois, K. Fritscher, and U. Schulz, EB-PVD processing of pyrochlore-structured La₂Zr₂O₇-based TBCs, *Surf. Coat. Technol.* **182**, 175 (2004).
- [63] J. Zhang, X. Guo, Y.-G. Jung, L. Li, and J. Knapp, Lanthanum zirconate based thermal barrier coatings: A review, *Surf. Coat. Technol.* **323**, 18 (2017).
- [64] M. Simoncelli, N. Marzari, and F. Mauri, Wigner formulation of thermal transport in solids, *Phys. Rev. X* **12**, 041011 (2022).
- [65] B. Winkler, V. Milman, E. V. Akhmatkaya, and R. H. Nobes, Bonding and dynamics of Mg in pyrope: a theoretical investigation, *Am. Mineral.* **85**, 608 (2000).
- [66] Y. Hu, Z. Wu, P. K. Dera, and C. R. Bina, Thermodynamic and elastic properties of pyrope at high pressure and high temperature by first-principles calculations, *J. Geophys. Res.: Solid Earth* **121**, 6462 (2016).
- [67] R. Destro, R. Ruffo, P. Roversi, R. Soave, L. Loconte, and L. Lo Presti, Anharmonic motions versus dynamic disorder at the Mg ion from the charge densities in pyrope (Mg₃Al₂Si₃O₁₂) crystals at 30 K: six of one, half a dozen of the other, *Acta Crystallogr., Sect. B* **73**, 722 (2017).
- [68] D. Nuzhnyy, J. Petzelt, M. Savinov, T. Ostapchuk, V. Bovtun, M. Kempa, J. Hlinka, V. Buscaglia, M. T. Buscaglia, and P. Nanni, Broadband dielectric response of Ba(Zr, Ti)O₃ ceramics: From incipient via relaxor and diffuse up to classical ferroelectric behavior, *Phys. Rev. B* **86**, 014106 (2012).
- [69] Y. Liu, W. Zhang, B. Wang, L. Sun, F. Li, Z. Xue, G. Zhou, B. Liu, and H. Nian, Theoretical and experimental investigations

- on high temperature mechanical and thermal properties of BaZrO₃, *Ceram. Int.* **44**, 16475 (2018).
- [70] S. Yamanaka, K. Kurosaki, T. Maekawa, T. Matsuda, S.-I. Kobayashi, and M. Uno, Thermochemical and thermophysical properties of alkaline-earth perovskites, *J. Nucl. Mater.* **344**, 61 (2005).
- [71] F. Nakamori, Y. Ohishi, H. Muta, K. Kurosaki, K.-I. Fukumoto, and S. Yamanaka, Mechanical and thermal properties of ZrSiO₄, *J. Nucl. Sci. Technol.* **54**, 1267 (2017).
- [72] J. Zheng, D. Shi, Y. Yang, C. Lin, H. Huang, R. Guo, and B. Huang, Anharmonicity-induced phonon hardening and phonon transport enhancement in crystalline perovskite BaZrO₃, *Phys. Rev. B* **105**, 224303 (2022).
- [73] T. Zhu and E. Ertekin, Mixed phononic and non-phononic transport in hybrid lead halide perovskites: glass-crystal duality, dynamical disorder, and anharmonicity, *Energy Environ. Sci.* **12**, 216 (2019).
- [74] F. Eriksson, E. Fransson, and P. Erhart, The HIPHIVE package for the extraction of high-order force constants by machine learning, *Adv. Theor. Simul.* **2**, 1800184 (2019).
- [75] D. J. Voneshen, M. C. Hatnean, T. G. Perring, H. C. Walker, K. Refson, G. Balakrishnan, and J. P. Goff, Kagome modes, a new route to ultralow thermal conductivity? [arXiv:1809.06265](https://arxiv.org/abs/1809.06265).
- [76] P. Rosander, E. Fransson, C. Milesi-Brault, C. Toulouse, F. Bourdarot, A. Piovano, A. Bossak, M. Guennou, and G. Wahnström, Anharmonicity of the antiferrodistortive soft mode in barium zirconate BaZrO₃, *Phys. Rev. B* **108**, 014309 (2023).
- [77] W. Li and N. Mingo, Thermal conductivity of fully filled skutterudites: Role of the filler, *Phys. Rev. B* **89**, 184304 (2014).
- [78] F. Knoop, T. A. R. Purcell, M. Scheffler, and C. Carbogno, Anharmonicity measure for materials, *Phys. Rev. Mater.* **4**, 083809 (2020).
- [79] L. Dong, D. S. Stone, and R. S. Lakes, Enhanced dielectric and piezoelectric properties of $x\text{BaZrO}_3 - (1 - x)\text{BaTiO}_3$ ceramics, *J. Appl. Phys.* **111**, 084107 (2012).
- [80] K. W. Schlichting, N. P. Padture, and P. G. Klemens, Thermal conductivity of dense and porous yttria-stabilized zirconia, *J. Mater. Sci.* **36**, 3003 (2001).
- [81] S.-H. Guan, C. Shang, and Z.-P. Liu, Resolving the temperature and composition dependence of ion conductivity for yttria-stabilized zirconia from machine learning simulation, *J. Phys. Chem. C* **124**, 15085 (2020).
- [82] N. Nitani, T. Yamashita, T. Matsuda, S.-I. Kobayashi, and T. Ohmichi, Thermophysical properties of rock-like oxide fuel with spinel–yttria stabilized zirconia system, *J. Nucl. Mater.* **274**, 15 (1999).
- [83] H. Cynn, O. L. Anderson, and M. Nicol, Effects of cation disordering in a natural MgAl₂O₄ spinel observed by rectangular parallelepiped ultrasonic resonance and Raman measurements, *Pure Appl. Geophys.* **141**, 415 (1993).
- [84] I. Ganesh, A review on magnesium aluminate (MgAl₂O₄) spinel: synthesis, processing and applications, *Int. Mater. Rev.* **58**, 63 (2013).
- [85] W. A. Fischer, D. Janke, and M. Schulenburg, Keramische und elektrolytische Eigenschaften von Zirkonsilicat ZrSiO₄ bei Temperaturen um 1600 °C, *Arch. Eisenhüttenwes.* **47**, 607 (1976).
- [86] J. Sakihama and R. Salomão, Microstructure development in porous calcium hexaluminate and application as a high-temperature thermal insulator: A critical review, *Interceram - Int. Ceram. Rev.* **68**, 58 (2019).
- [87] K. Vishista, F. D. Gnanam, and H. Awaji, Sol-Gel synthesis and characterization of alumina-calcium hexaaluminate composites, *J. Am. Ceram. Soc.* **88**, 1175 (2005).
- [88] L. Thiéblot, J. Roux, and P. Richet, High-temperature thermal expansion and decomposition of garnets, *Eur. J. Mineral.* **10**, 7 (1998).
- [89] K.-I. Horai, Thermal conductivity of rock-forming minerals, *J. Geophys. Res.* **76**, 1278 (1971).
- [90] D. Li, X. Xu, H. Zhu, X. Chen, W. D. Tan, J. Zhang, D. Tang, J. Ma, F. Wu, C. Xia, and J. Xu, Characterization of laser crystal Yb:CaYAlO₄, *J. Opt. Soc. Am. B* **28**, 1650 (2011).
- [91] E. F. Kustov, V. P. Petrov, D. S. Petrova, and J. P. Udalov, Absorption and luminescence spectra of Nd³⁺ and Er³⁺ ions in monocrystals of CaYAlO₄, *Physica Status Solidi (a)* **41**, 379 (1977).
- [92] K. Omoto and M. Yashima, Origin of anisotropic thermal expansion in CaYAlO₄, *Appl. Phys. Express* **7**, 037301 (2014).
- [93] N. P. Padture and P. G. Klemens, Low thermal conductivity in garnets, *J. Am. Ceram. Soc.* **80**, 1018 (1997).
- [94] H. Furuse, R. Yasuhara, and K. Hiraga, Thermo-optic properties of ceramic YAG at high temperatures, *Opt. Mater. Express* **4**, 1794 (2014).
- [95] W. Buykx, Specific heat, thermal diffusivity and thermal conductivity of synroc, perovskite, zirconolite and barium hollandite, *J. Nucl. Mater.* **107**, 78 (1982).
- [96] M. Jafar, S. Phapale, S. N. Achary, R. Mishra, and A. K. Tyagi, High-temperature crystallographic and thermodynamic investigations on synthetic zirconolite (CaZrTi₂O₇), *J. Therm. Anal. Calorim.* **131**, 2709 (2018).
- [97] K. M. Manu, C. Karthik, R. Ubic, and M. T. Sebastian, Effect of Ca²⁺ substitution on the structure, microstructure, and microwave dielectric properties of Sr₂Al₂SiO₇ Ceramic, *J. Am. Ceram. Soc.* **96**, 3842 (2013).
- [98] M. Merlini, M. Gemmi, and G. Artioli, Thermal expansion and phase transitions in åkermanite and gehlenite, *Phys. Chem. Miner.* **32**, 189 (2005).
- [99] W. Ma, D. Mack, J. Malzbender, R. Vaßen, and D. Stöver, Yb₂O₃ and Gd₂O₃ doped strontium zirconate for thermal barrier coatings, *J. Eur. Ceram. Soc.* **28**, 3071 (2008).
- [100] Y. Li, Z. Jia, Y. Yin, Q. Hu, W. Mu, J. Zhang, X. Yu, and X. Tao, Temperature dependence of the thermal, electrical resistivity, dielectric and piezoelectric properties of CaYAl₃O₇ Crystal, *Crystals* **8**, 34 (2018).
- [101] C. Wan, T. D. Sparks, P. Wei, and D. R. Clarke, Thermal conductivity of the rare-earth strontium aluminates, *J. Am. Ceram. Soc.* **93**, 1457 (2010).
- [102] J. Feng, B. Xiao, R. Zhou, W. Pan, and D. R. Clarke, Anisotropic elastic and thermal properties of the double perovskite slab-rock salt layer Ln₂SrAl₂O₇ (Ln = La, Nd, Sm, Eu, Gd or Dy) natural superlattice structure, *Acta Mater.* **60**, 3380 (2012).
- [103] J. Yang, X. Qian, W. Pan, R. Yang, Z. Li, Y. Han, M. Zhao, M. Huang, and C. Wan, Diffused lattice vibration and ultralow thermal conductivity in the binary Ln–Nb–O Oxide System, *Adv. Mater.* **31**, 1808222 (2019).
- [104] A. Mielewczyk-Gryń, P. Winiarz, S. Wachowski, and M. Gazda, High-temperature properties of titanium-substituted yttrium niobate, *J. Mater. Res.* **34**, 3312 (2019).

- [105] A. Iakovleva, Study of novel proton conductors for high temperature solid oxide cells, Ph.D. thesis, Université Paris-Saclay (ComUE) (2015).
- [106] X. Fu, E. G. VÍllora, Y. Matsushita, Y. Kitanaka, Y. Noguchi, M. Miyayama, K. Shimamura, and N. Ohashi, Influence of oxygen partial pressure during growth on optical and electrical properties of $\text{Ca}_3\text{TaAl}_3\text{Si}_2\text{O}_{14}$ single crystals, *Cryst. Growth Des.* **16**, 2151 (2016).
- [107] Q. Zhou, B. J. Kennedy, and J. A. Kimpton, The effect of disorder in Ba_2YTao_6 on the tetragonal to cubic phase transition, *J. Solid State Chem.* **184**, 729 (2011).
- [108] X. Zhou, Z. Xu, X. Fan, S. Zhao, X. Cao, and L. He, $\text{Y}_4\text{Al}_2\text{O}_9$ ceramics as a novel thermal barrier coating material for high-temperature applications, *Mater. Lett.* **134**, 146 (2014).
- [109] Y. Zhou, X. Lu, H. Xiang, and Z. Feng, Preparation, mechanical, and thermal properties of a promising thermal barrier material: $\text{Y}_4\text{Al}_2\text{O}_9$, *J. Adv. Ceram.* **4**, 94 (2015).
- [110] W. Ma and H. Dong, Ceramic thermal barrier coating materials, in *Thermal Barrier Coatings* (Elsevier, 2011), pp. 25–52.
- [111] L. Guo, H. Guo, G. Ma, S. Gong, and H. Xu, Phase stability, microstructural and thermo-physical properties of $\text{BaLn}_2\text{Ti}_3\text{O}_{10}$ ($\text{Ln} = \text{Nd}$ and Sm) ceramics, *Ceram. Int.* **39**, 6743 (2013).
- [112] L. Guo, H. Guo, G. Ma, M. Abbas, and S. Gong, Ruddlesden–Popper structured $\text{BaLa}_2\text{Ti}_3\text{O}_{10}$, a highly anisotropic material for thermal barrier coatings, *Ceram. Int.* **38**, 4345 (2012).
- [113] Y. Pan, B. Liang, Y. Niu, D. Han, D. Liu, and X. Zheng, Research on thermal stability and properties of $\text{Ca}_3\text{ZrSi}_2\text{O}_9$ as potential T/EBC materials, *Coatings* **11**, 583 (2021).
- [114] D. Jiang, D. Ekren, F. Azough, S. J. Day, K. Chen, A. Mahajan, D. M. Kepaptsoglou, Q. M. Ramasse, M. J. Reece, and R. Freer, The structure and thermoelectric properties of tungsten bronze $\text{Ba}_6\text{Ti}_2\text{Nb}_8\text{O}_{30}$, *J. Appl. Phys.* **126**, 125115 (2019).
- [115] R. Hopkins, N. Melamed, T. Henningsen, and G. Roland, Crystal growth and properties of $\text{CaY}_4(\text{SiO}_4)_3\text{O}$, a new laser host for Ho^{+3} , *J. Cryst. Growth* **10**, 218 (1971).
- [116] R. Vaßen, G. Kerkhoff, and D. Stöver, Development of a micromechanical life prediction model for plasma sprayed thermal barrier coatings, *Mater. Sci. Eng.* **303**, 100 (2001).
- [117] J. F. Nye *et al.*, *Physical Properties of Crystals: Their Representation by Tensors and Matrices* (Oxford University Press, 1985).
- [118] L. Wang, J. D. Lee, and C.-D. Kan, Work conjugate pair of stress and strain in molecular dynamics, *Int. J. Smart Nano Mater.* **7**, 144 (2016).
- [119] W. Voigt, *Lehrbuch der Kristallphysik (mit ausschluß der kristalloptik)* (B.G. Teubner, Leipzig, Berlin, 1910).
- [120] A. Reuss, Berechnung der Fließgrenze von Mischkristallen auf Grund der Plastizitätsbedingung für Einkristalle, *Z. Angew. Math. Mech.* **9**, 49 (1929).
- [121] R. Hill, The elastic behaviour of a crystalline aggregate, *Proc. Phys. Soc. A* **65**, 349 (1952).
- [122] C. L. Wan, W. Pan, Q. Xu, Y. X. Qin, J. D. Wang, Z. X. Qu, and M. H. Fang, Effect of point defects on the thermal transport properties of $(\text{La}_x\text{Gd}_{1-x})_2\text{Zr}_2\text{O}_7$: Experiment and theoretical model, *Phys. Rev. B* **74**, 144109 (2006).
- [123] D. de Ligny and P. Richet, High-temperature heat capacity and thermal expansion of SrTiO_3 and SrZrO_3 perovskites, *Phys. Rev. B* **53**, 3013 (1996).
- [124] S. V. Sinogeikin and J. D. Bass, Single-crystal elasticity of pyrope and MgO to 20 GPa by Brillouin scattering in the diamond cell, *Phys. Earth Planet. Inter.* **120**, 43 (2000).
- [125] P. Kumar and I. Adlakha, Effect of interstitial hydrogen on elastic behavior of metals: An ab-initio study, *J. Eng. Mater. Technol.* **145**, 011003 (2023).
- [126] P. Mishra, P. Kumar, L. Neelakantan, and I. Adlakha, First-principles prediction of electrochemical polarization and mechanical behavior in Mg based intermetallics, *Comput. Mater. Sci.* **214**, 111667 (2022).
- [127] S. Pugh, XCII. Relations between the elastic moduli and the plastic properties of polycrystalline pure metals, *Lond. Edinb. Dublin Philos. Mag. J. Sci.* **45**, 823 (1954).
- [128] J. J. Gilman, *Electronic Basis of the Strength of Materials* (Cambridge University Press, 2003).
- [129] I. Zacharov, R. Arslanov, M. Gunin, D. Stefonishin, A. Bykov, S. Pavlov, O. Panarin, A. Maliutin, S. Rykovanov, and M. Fedorov, “Zhores”—Petaflops supercomputer for data-driven modeling, machine learning and artificial intelligence installed in Skolkovo Institute of Science and Technology, *Open Eng.* **9**, 512 (2019).